

## JGR Solid Earth

## RESEARCH ARTICLE

10.1029/2021JB022098

## Key Points:

- Inelastic wedge deformation produces impulsive tsunami due to short wavelength of seafloor uplift
- A simple inelastic wedge deformation model can explain the large runup of the 1896 Sanriku tsunami
- The impulsive tsunami and large runup along the Sanriku coast in 2011 can be due to inelastic deformation north of 38.5°N

## Supporting Information:

Supporting Information may be found in the online version of this article.

## Correspondence to:

Y. Du,  
[ydu0755@sdsu.edu](mailto:ydu0755@sdsu.edu)

## Citation:

Du, Y., Ma, S., Kubota, T., & Saito, T. (2021). Impulsive tsunami and large runup along the Sanriku coast of Japan produced by an inelastic wedge deformation model. *Journal of Geophysical Research: Solid Earth*, 126, e2021JB022098. <https://doi.org/10.1029/2021JB022098>

Received 19 MAR 2021

Accepted 29 JUL 2021

# Impulsive Tsunami and Large Runup Along the Sanriku Coast of Japan Produced by an Inelastic Wedge Deformation Model

Yue Du<sup>1,2</sup> , Shuo Ma<sup>1</sup> , Tatsuya Kubota<sup>3</sup> , and Tatsuhiko Saito<sup>3</sup> 

<sup>1</sup>Department of Geological Sciences, San Diego State University, San Diego, CA, USA, <sup>2</sup>Scripps Institution of Oceanography, University of California, San Diego, CA, USA, <sup>3</sup>National Research Institute for Earth Science and Disaster Resilience, Tsukuba, Japan

**Abstract** Dynamic wedge failure produces short-wavelength seafloor uplift efficiently with diminishing shallow slip on the plate interface, generating impulsive tsunami. For ria coasts with prevalent small-wavelength bathymetric and geomorphologic features, such as the Sanriku coast of Japan, impulsive tsunami can be amplified to produce large runup. We model tsunami propagation and runup of the 1896 Sanriku tsunami by using the seafloor deformation from dynamic rupture models of Ma and Nie (2019) for a  $M_W$  8 earthquake with inelastic wedge deformation. The nonlinear Boussinesq equation is solved by a nested-grid finite-difference method with high-resolution bathymetry data. We show that an inelastic deformation model with extensive wedge failure produces impulsive tsunami similar to those observed offshore the Sanriku coast in the 2011 Tohoku earthquake and generates large runup remarkably consistent with the 1896 Sanriku tsunami. As an alternative to previous models based solely on fault slip, we suggest that the impulsive tsunami and large runup along the Sanriku coast observed in the 2011 Tohoku earthquake can be explained by inelastic wedge deformation north of 38.5°N.

**Plain Language Summary** The Sanriku coast hosted several of the most devastating tsunami in recorded history of Japan, including the 1896 Sanriku tsunami and 2011 Tohoku tsunami. The runup on the Sanriku coast in both tsunamis were up to 40 m. It is unclear why such large runup can occur. Large near-trench slip north of 38.5°N in the Japan Trench were inferred to generate the devastating 2011 tsunami on the Sanriku coast, which is, however, inconsistent with the bathymetry observations. Here we show that the inelastic failure of wedge sediments north of 38.5°N due to dynamic stress can generate efficient short-wavelength seafloor uplift with diminishing slip at the trench, consistent with the bathymetry observations, which produces impulsive (short-period) tsunami that can be amplified by the rugged Sanriku coast. An inelastic wedge deformation model of the 1896 Sanriku earthquake is shown to generate impulsive tsunami similar to what was observed offshore the Sanriku coast in the 2011 Tohoku tsunami and produce tsunami runup remarkably consistent with the observed runup of the 1896 Sanriku tsunami. Dynamic failure of thick wedge sediments north of 38.5°N in the Japan Trench likely plays an important role in the generation of the devastating 2011 Tohoku tsunami.

## 1. Introduction

The ria coast of Sanriku region, situated about 50–200 km north of the Sendai Plain, witnessed several of the worst tsunamis in recorded history of Japan (Figure 1). The 1896 Sanriku earthquake, a  $\sim M_W$  8 tsunami earthquake (e.g., Kanamori, 1972; Satake et al., 2017; Tanioka & Satake, 1996; Tanioka & Seno, 2001), generated weak high-frequency ground shaking, but the resulting tsunami produced runup up to 38.2 m on the Sanriku coast, causing about 22,000 deaths (Shuto et al., 2007). The Sanriku coast was hit by another tsunami due to a  $M_W$  8.4 outer rise earthquake in 1933 with runup as high as 28.7 m (e.g., Abe, 1978; Kanamori, 1971; Mori et al., 2011). In the 2011  $M_W$  9.0 Tohoku earthquake the largest tsunami runup heights (up to 40 m) were observed on the Sanriku coast (Mori et al., 2011, Figure 2), causing catastrophic destructions more than 100 km north of the epicenter ( $\sim 38.1^\circ\text{N}$ ). However, the largest shallow slip near the trench (more than 50 m) was observed (Fujiwara et al., 2011; Kodaira et al., 2020) or inferred from most inversion models (Lay, 2018, and references therein) updip from the hypocenter. The maximum tsunami

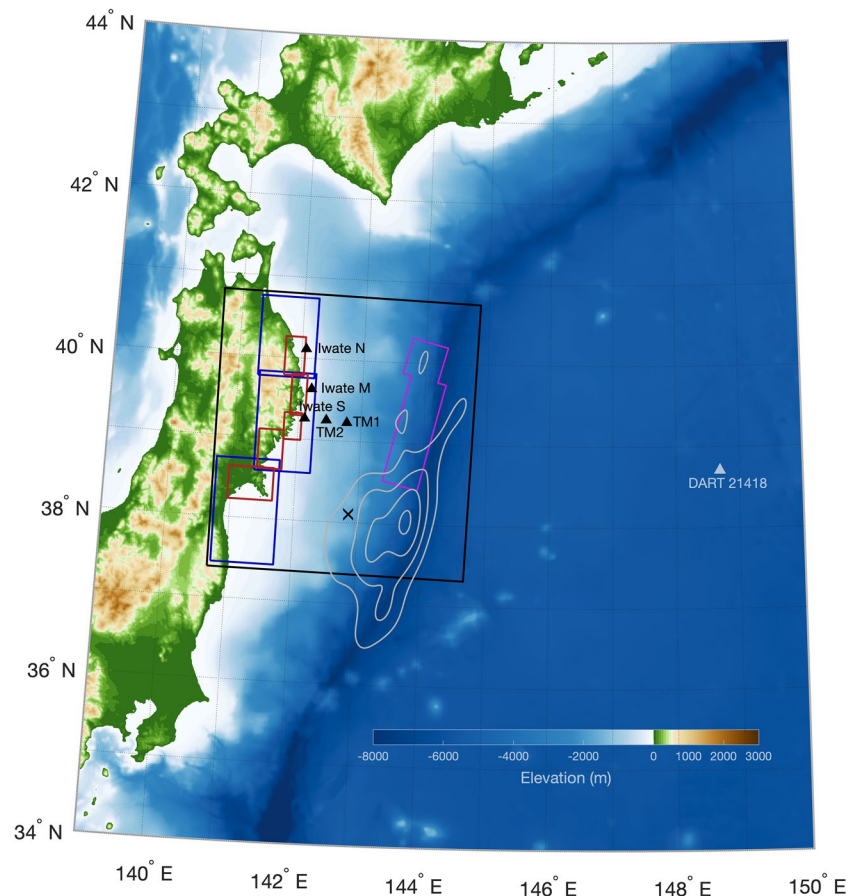


**Figure 1.** Map of the region of interest in this study. Four nested grid layers are used in the computational domain. The outmost grid layer uses 1350 m grid spacing with 974 x 1370 grid cells, covering the entire computational domain (larger than shown here). The black rectangle shows the 450 m grid. Three overlapping blue rectangles denote the 150 m grid. The 50 m grid is shown by five red overlapping rectangles, covering the Sanriku coast in high resolution. The six triangles denote the stations used in this study. The cross symbol marks the epicenter of the 2011 Tohoku earthquake. The contours are the initial sea surface elevation model of Saito et al. (2014) for the 2011 Tohoku tsunami, showing the long-wavelength seafloor uplift mostly south of 39°N. The magenta outlines are the surface projection of the fault plane used in Satake et al. (2017) for the 1896 Sanriku earthquake, which is model III of this work.

runup heights are quite similar on the Sanriku coast between the 1896 and 2011 earthquakes despite their different magnitudes (Figure 2).

Why does the Sanriku coast host such devastating tsunamis? Why did the largest tsunami in the 2011 Tohoku earthquake occur more than 100 km north of the largest shallow slip region (near 38.1°N)? In order to explain the large tsunami runup on the Sanriku coast, elastic dislocation models require large shallow slip (up to 36 m) near the trench north of ~38.5°N (e.g., Satake et al., 2013; Yamazaki et al., 2018). However, differential bathymetry data before and after the earthquake around 39.2°–39.5°N indicated no large shallow slip near the trench (Fujiwara et al., 2017; Kodaira et al., 2020). The bathymetry data also ruled out the possibility of a large submarine landslide (Tappin et al., 2014).

Without large shallow slip at trench or submarine landslide what caused the devastating tsunami along the Sanriku coast in the 2011 Tohoku earthquake? This is a major unresolved question related to the 2011 Tohoku earthquake despite unprecedented onshore and offshore data and numerous published models in the last 10 years (Kodaira et al., 2021). This question challenges current understanding of the fundamental physics of tsunamigenesis and needs to be critically addressed, which will be instrumental in evaluating and reducing tsunami hazard in the Japan Trench and other subduction zones worldwide. The prevailing hypothesis of large shallow slip in explaining tsunami generation is based on elastic dislocation theory,

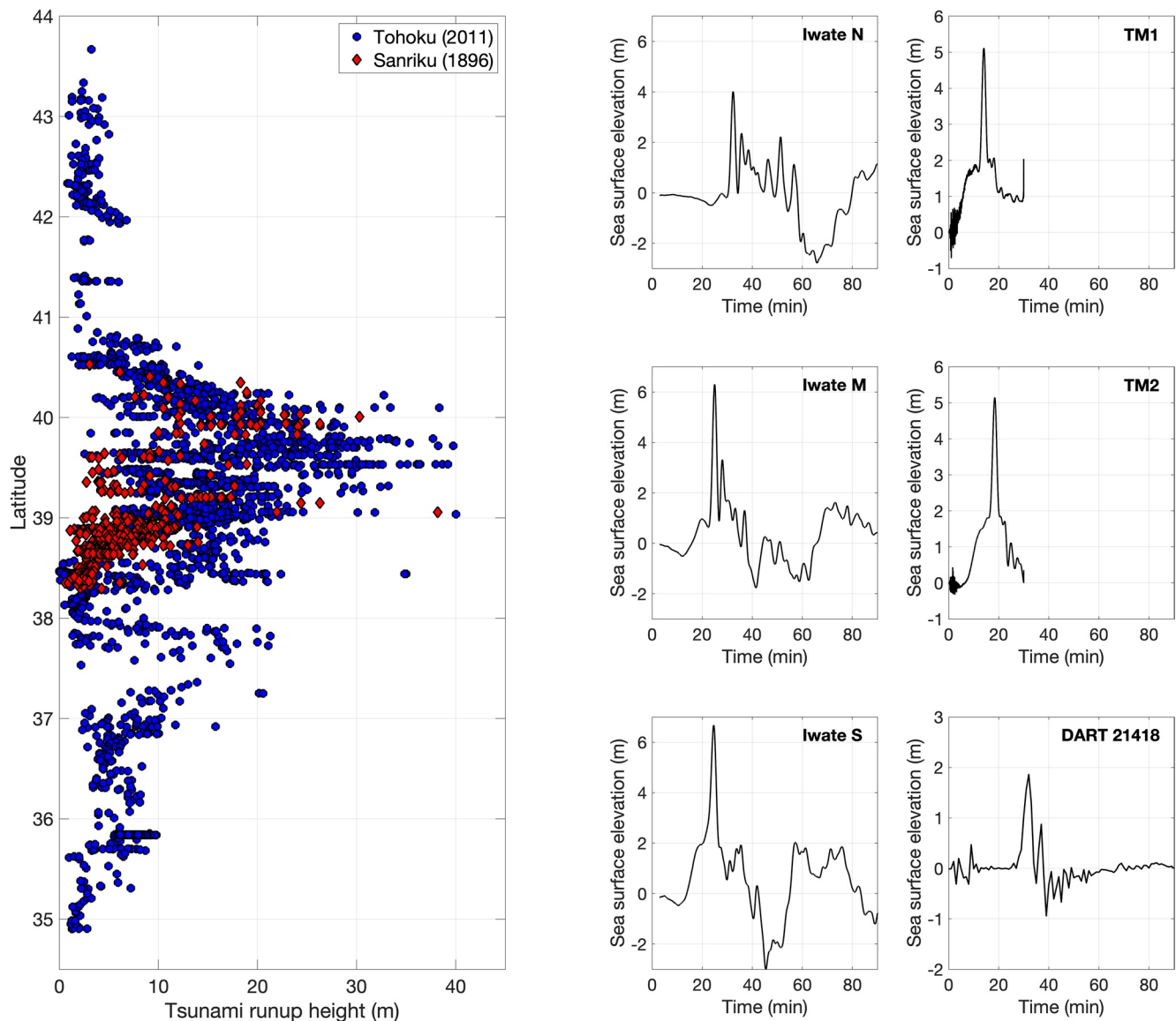


**Figure 2.** (Left) Comparison of observed tsunami runup heights in the 1896 Sanriku earthquake (Iki, 1897; Matsuo, 1933) and 2011 Tohoku earthquake (Mori et al., 2011). Both earthquakes produced large runup up to 40 m on the Sanriku coast despite different earthquake magnitudes. The 2011 tsunami height is consistently larger on the Sanriku coast more than 100 km north of the epicenter (38.1°N). (Right) Observed tsunami waveforms at six stations (shown in Figure 1) in the 2011 Tohoku earthquake. Five stations offshore of the Sanriku coast recorded a rare impulsive signal atop a broad regional signal. A deep-sea buoy station (DART 21418) recorded clear dispersive tsunami. The physics of producing these signals is addressed in this work.

which may not be applicable in shallow subduction zones with thick sediments and therefore cannot reconcile with these key observations in the 2011 Tohoku earthquake. We refer the reader to Ma and Nie (2019) and Wilson and Ma (2021) for more detailed discussion of physical mechanisms of tsunamigenesis and possible issues associated with elastic dislocation models.

Fujiwara et al. (2017) suggested that differential bathymetry data is more consistent with widespread inelastic deformation of wedge sediments (Tanioka & Seno, 2001). Ma (2012) and Ma and Hirakawa (2013) modeled inelastic wedge deformation in 2D dynamic rupture models of shallow subduction earthquakes by using the undrained Mohr-Coulomb plasticity theory. They showed that inelastic wedge deformation is more efficient to generate seafloor uplift than large shallow slip on a shallow dipping fault due to frictional sliding on conjugate Coulomb microfractures with steeper dips (the efficiency is defined by peak seafloor uplift scaled by seismic potency). With significant inelastic deformation large seafloor uplift occurs landward

from the trench with diminishing shallow slip on the fault, which is consistent with the observation of Fujiwara et al. (2017). Inelastic deformation is also a large energy sink (Ma & Hirakawa, 2013), which can lead to slow rupture velocity, deficiency of high-frequency seismic radiation, and low moment-scaled radiated energy, observed anomalously for tsunami earthquakes and in the shallow rupture characteristics of large tsunamigenic earthquakes (e.g., Lay et al., 2012).

Ma and Nie (2019) extended the inelastic wedge deformation model to 3D and modeled a  $M_w$  8.0 shallow subduction earthquake, similar to the 1896 Sanriku earthquake. They showed that along-strike variation of sediment thickness (thus wedge strength), such as in the Japan Trench (Kodaira et al., 2017; Tsuru et al., 2002), can cause along-strike variation of inelastic wedge deformation. In particular, they suggested that due to thick sediments north of 38.5°N inelastic deformation of sedimentary wedge can produce large seafloor uplift with diminishing shallow slip. In contrast, the scarcity of sediments in the south (near 38.1°N) induces mostly elastic wedge deformation, generating large shallow slip and mostly horizontal seafloor displacement but small uplift near the trench. Although the horizontal seafloor displacement can significantly contribute to tsunami generation (e.g., Tanioka & Satake, 1996) the efficiency of generating seafloor uplift (uplift normalized by slip) can be limited by the overall gentle slope of seafloor. The along-strike variations of shallow slip and seafloor uplift near the trench in the model are similar to the observations in the 2011 Tohoku earthquake (Fujiwara et al., 2011, 2017; Mori et al., 2011), suggesting a plausible mechanism for both large slip at the trench near 38.1°N and the devastating tsunami on the Sanriku coast without large northern trench slip in the 2011 Tohoku earthquake.

Another rare and intriguing observation in the 2011 Tohoku tsunami is that two ocean bottom pressure gauges (TM1 and TM2) and three GPS wave gauges off the Sanriku coast (Iwate N, M, and S) recorded an impulsive tsunami signal on top of a broad signal due to high sampling rates of the instruments (Figure 2). The impulsive signal was not observed south of the Sanriku coast. The broad signal is due to long-wavelength seafloor uplift caused by deep slip on a ~200 km wide fault south of ~39°N (e.g., Satake et al., 2013), which can be seen by the contours in Figure 1. The nature of the impulsive signal, however, is not well understood. The width of the impulsive signal is approximately 3–4 min at TM1 and TM2, which was thought to be caused by large localized slip at the trench near 38.1°N (e.g., Maeda et al., 2011). Later tsunami inversions (e.g., Satake et al., 2013; Yamazaki et al., 2018) attributed the impulsive signal to large near-trench slip north of 38.5°N. Tappin et al. (2014) fit the impulsive signals and runup on the Sanriku coast by using a submarine landslide model. As mentioned previously, all these models are inconsistent with the bathymetry observations of Fujiwara et al. (2017).

In this study, we will show that such impulsive tsunami signals can be a direct result of short-wavelength seafloor uplift produced by inelastic wedge deformation. Several studies (e.g., Shimozone et al., 2012, 2014; Yamanaka & Nakamura, 2020; Yamazaki et al., 2018) showed that the rugged Sanriku coast, characterized by steep terrains and narrow and long bays, can greatly amplify the impulsive (short-period) tsunami to cause large runup, although local amplification patterns can be highly nonlinear (e.g., Rogers & Mei, 1978). The amplification of long-period tsunami on the Sanriku coast due to long-wavelength seafloor uplift south of ~39°N in the 2011 Tohoku earthquake was found to be significantly less (e.g., Yamanaka & Nakamura, 2020). This frequency-dependent amplification on the Sanriku coast may explain why the short-wavelength tsunami of the 1896 and 1933 Sanriku earthquakes produced similar runup to the 2011 Tohoku earthquake despite their different magnitudes. Below we will show acute sensitivity of the runup on the Sanriku coast to impulsive tsunami generated by inelastic wedge deformation. Thus, inelastic wedge deformation is a mechanism that can explain both the impulsive tsunami and large runup along the Sanriku coast without large trench slip, consistent with what was observed in the 2011 Tohoku earthquake.

To demonstrate that inelastic wedge deformation can produce impulsive tsunami, we will model the 1896 Sanriku tsunami by using the seafloor displacements from two models of Ma and Nie (2019) as the initial conditions. The models represent  $M_w$  8 shallow subduction earthquakes, with fault geometry and rupture extent similar to that of Tanioka and Seno (2001) for the 1896 Sanriku earthquake. One slight difference is that Ma and Nie (2019) included a seafloor slope, while Tanioka and Seno (2001) used a flat seafloor and a buried fault. One of the Ma and Nie models has mostly elastic wedge response with large shallow slip at the trench and mostly horizontal seafloor displacement (Figure 3). The second Ma and Nie model (Figure 4) has significant inelastic wedge deformation, which generates narrow and large uplift landward from



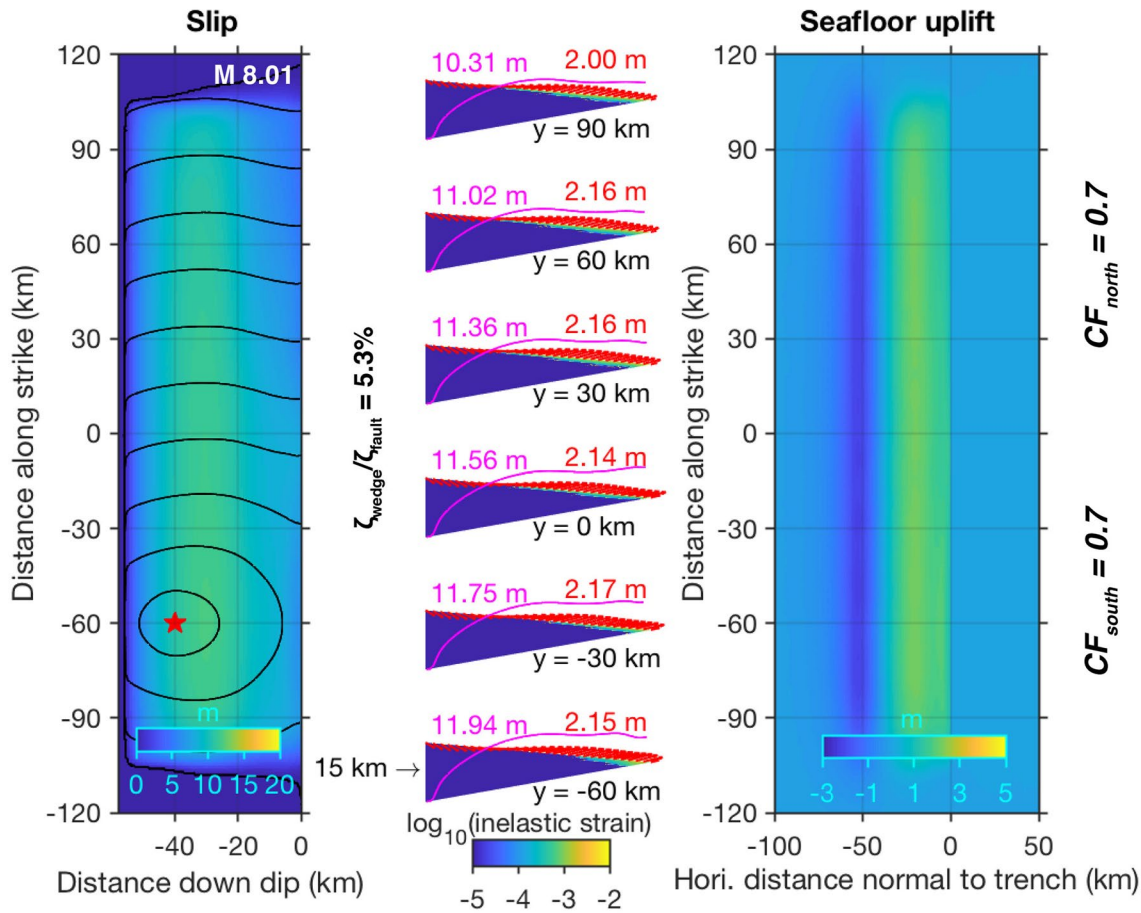


**Figure 3.** The large shallow slip model and model I of this work. Left panel shows the slip distribution on the fault with moment magnitude shown on the upper right corner and rupture time contours every 10 s. The middle panel shows the final seafloor displacement (red arrows), on-fault slip (magenta curves), and inelastic shear strain at six cross sections ( $y$  is distance along strike). The numbers in red and magenta denote the peak uplift and slip, respectively, at each cross section. The ratio of seismic potency in the wedge to the fault is shown between the first two panels. The right panel shows the surface map of final vertical seafloor displacement. Figure from Ma and Nie (2019). CF: closeness-to-failure.

the trench with diminishing shallow slip. Such narrow uplift will be shown to directly lead to impulsive tsunami similar to those observed in 2011. The differences between these two models are due to different wedge strengths, characterized by a closeness-to-failure ( $CF$ ) parameter. The  $CF$  is defined as the ratio of square root of second invariant of deviatoric stress tensor to yield stress in a Drucker-Prager yield criterion (see equation 3 of Ma & Nie, 2019), which is between 0 and 1. The  $CF$  of 0.7 and 0.95 were used everywhere in the wedge in Figures 3 and 4, respectively. As the  $CF$  increases, the wedge is less cohesive and closer to failure; wedge failure due to dynamic stresses during rupture propagation gives rise to significant inelastic deformation and distinctly different seafloor deformation.

Hereafter we will refer to the model in Figure 3 as model I and Figure 4 as model II. Model II is likely more applicable to the 1896 Sanriku earthquake due to the presence of thick sediments north of  $38.5^{\circ}\text{N}$  (Tsuru et al., 2002). The moment magnitudes ( $M_w$ ) for these two models are 8.01 and 7.95, respectively. More detailed discussion of the two models and how variation of sediment thickness may lead to along-arc variation of inelastic deformation in the Japan Trench can be found in Ma and Nie (2019). We will also consider a kinematic slip model of the 1896 Sanriku earthquake (based on elastic dislocation theory), which is the final model of Satake et al. (2017). The model ( $M_w$  8.1) consists of 8 subfaults with large localized buried slip (20 m) on two subfaults at depths of about 3.5–7 km, illustrated in Figure 5d. Each subfault is 50 km long and 25 km wide, with strike  $193^{\circ}$ , dip  $8^{\circ}$ , and rake  $81^{\circ}$ . We will refer to this model as model III in this study.

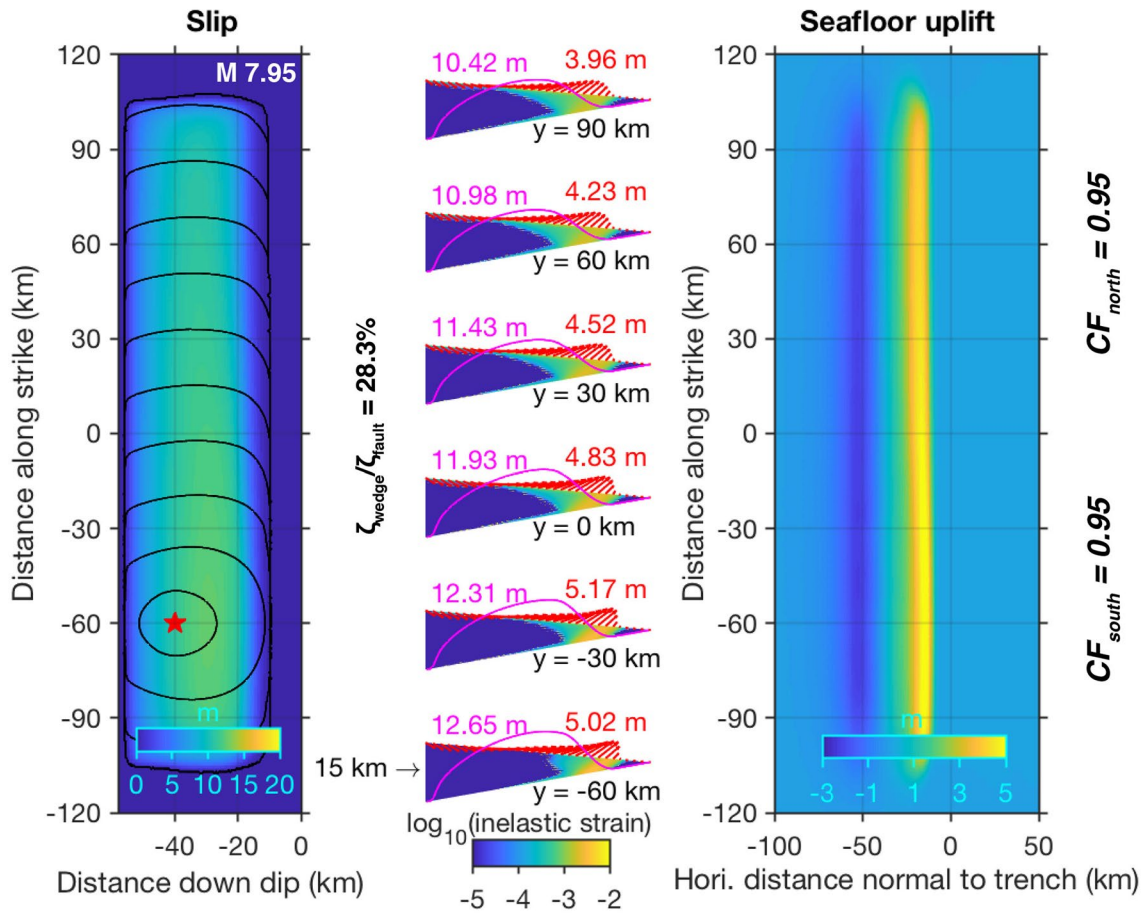


**Figure 4.** The inelastic wedge deformation model and model II of this work. Similar to Figure 3. The inelastic wedge deformation produces large and narrow seafloor uplift landward from trench with diminishing shallow slip. Figure from Ma and Nie (2019). CF: closeness-to-failure.

We will show that shorter-wavelength seafloor uplift of models II and III produce more impulsive tsunami signal than model I and the former are similar to the observed impulsive signal in the 2011 Tohoku tsunami. Neither model II or III has large trench slip, consistent with the observations of Fujiwara et al. (2017). However, model III may have a plausibility issue due to large stress change in the overriding wedge caused by large localized slip (e.g., Geist & Dmowska, 1999), which may lead to inelastic deformation violating the assumption of elastic dislocation. Model II produces large runup with a remarkable fit to the observed runup of the 1896 Sanriku tsunami (Iki, 1897; Matsuo, 1933) without any model tuning. Model I, with a longer-wavelength and smaller seafloor uplift, produces consistently lower tsunami height and runup than model II. The limited along-strike extent of localized buried slip of model III overestimates the runup of the 1896 tsunami between about 39.3°N and 39.9°N and underestimates the runup elsewhere. Given the capability of generating impulsive tsunami and large runup along the Sanriku coast by short-wavelength seafloor uplift we suggest that inelastic deformation of thick wedge sediments north of 38.5°N can likely explain the large tsunami runup on the Sanriku coast in the 2011 Tohoku earthquake while being consistent with the observations of Fujiwara et al. (2017).

## 2. Tsunami Modeling

We model the 1896 Sanriku tsunami by solving the nonlinear Boussinesq equation in a Cartesian coordinate system

$$\frac{\partial \eta}{\partial t} + \frac{\partial P}{\partial x} + \frac{\partial Q}{\partial y} = 0, \quad (1)$$

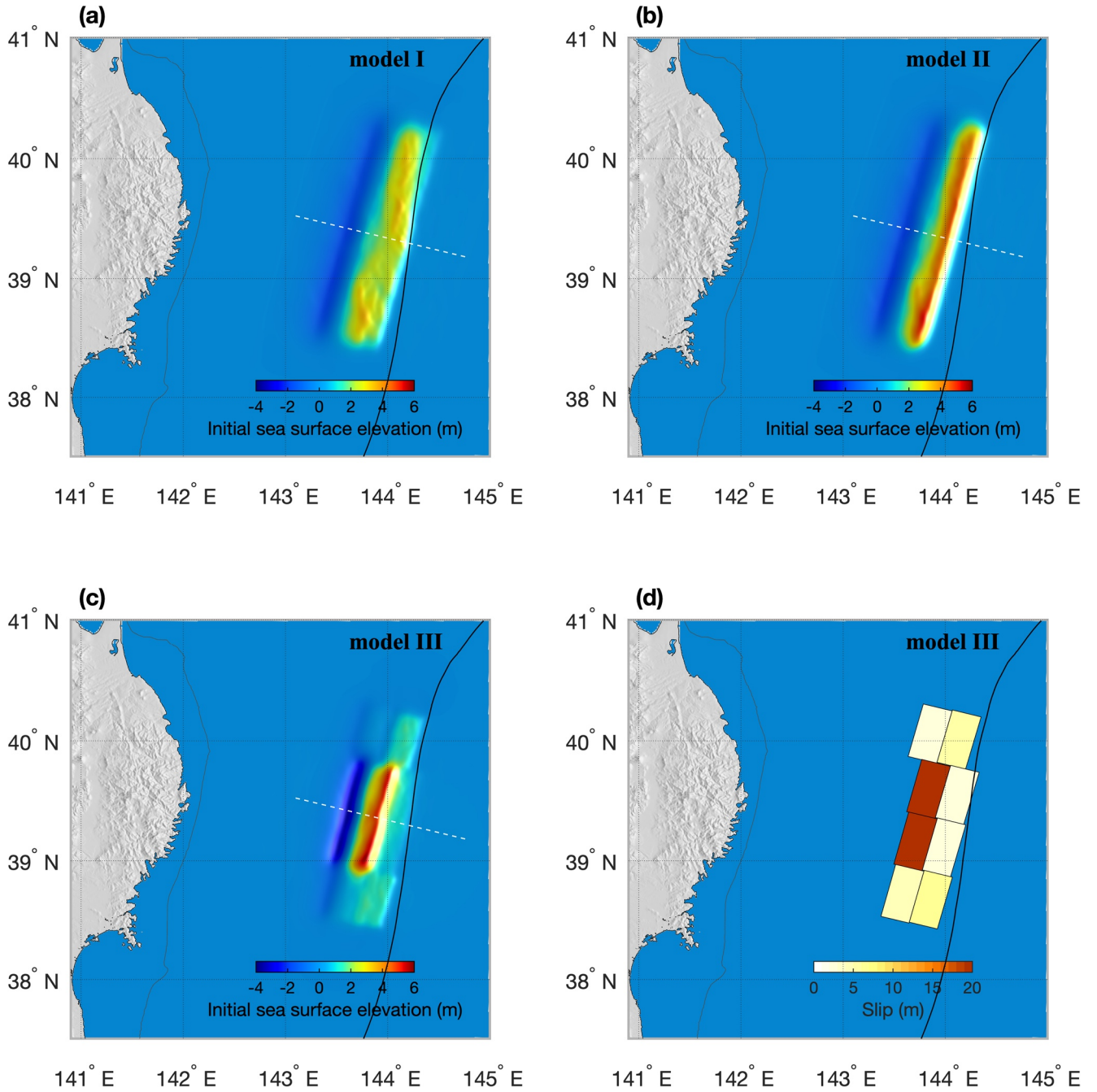


**Figure 5.** (a–c) Comparison of initial sea surface elevations among three models of the 1896 Sanriku tsunami in this study. Model III is the final model of Satake et al. (2017). The slip distribution of this model is shown in (d). The white dashed line marks the cross section shown in Figure 6. The thick black line depicts the trench. The thin gray line shows the 200 m-depth bathymetry contour, which marks approximately the boundary of continental shelf.

$$\frac{\partial P}{\partial t} + \frac{\partial}{\partial x} \left( \frac{P^2}{H} \right) + \frac{\partial}{\partial y} \left( \frac{PQ}{H} \right) + gH \frac{\partial \eta}{\partial x} + \frac{gn^2}{H^{7/3}} P \sqrt{P^2 + Q^2} = \frac{H^2}{3} \frac{\partial}{\partial x} \frac{\partial}{\partial t} \left( \frac{\partial P}{\partial x} + \frac{\partial Q}{\partial y} \right), \quad (2)$$

$$\frac{\partial Q}{\partial t} + \frac{\partial}{\partial x} \left( \frac{PQ}{H} \right) + \frac{\partial}{\partial y} \left( \frac{Q^2}{H} \right) + gH \frac{\partial \eta}{\partial y} + \frac{gn^2}{H^{7/3}} Q \sqrt{P^2 + Q^2} = \frac{H^2}{3} \frac{\partial}{\partial y} \frac{\partial}{\partial t} \left( \frac{\partial P}{\partial x} + \frac{\partial Q}{\partial y} \right), \quad (3)$$

where  $\eta$  is sea surface height,  $P$  and  $Q$  are volume fluxes in  $x$  and  $y$ , respectively,  $g$  is gravitational acceleration ( $9.8 \text{ m/s}^2$ ),  $H$  is total water depth ( $H = \eta + h$ ,  $h$  is initial ocean depth), and  $n$  is the Manning's sea bottom roughness coefficient. In this work, a constant Manning's coefficient  $n = 0.03 \text{ m}^{-\frac{1}{3}} \text{ s}$  is used throughout the model (e.g., Saito et al., 2014). The volume fluxes are given by  $P = v_x H$  and  $Q = v_y H$ , where  $v_x$  and  $v_y$  are depth-averaged flow velocities assuming shallow water. The governing equations written in terms of volume fluxes rather than velocities, known as the conservative form (e.g., Roeber et al., 2010; Wang & Power, 2011), have a wider range of applications even when the shallow-water assumptions are invalid, such as across a shock or hydraulic jump, and show better accuracy in areas with steep bathymetry gradients (Dresback et al., 2005). Baba et al. (2015) solved the similar equations in a spherical coordinate system.

The Boussinesq equation is widely used in modeling dispersive tsunami propagation (e.g., Baba et al., 2015; Horrillo et al., 2006; Hossen et al., 2015; Kirby et al., 2013; Saito et al., 2014; Tanioka et al., 2018; Tappin et al., 2014). The dispersion is due to the terms on the right side of Equations 2 and 3, which approximate true frequency dispersion reasonably well even when tsunami wavelength is not much larger than ocean depth (e.g., Saito, 2019). Baba et al. (2015) further showed that the nonlinear Equations 2 and 3 can simulate a remarkable near-coast small-wavelength phenomenon called "tsunami soliton fission," which is due to frequency dispersion as well as dispersion from wave amplitude (i.e., wave speed is a function of wave amplitude). Without the two right-side terms Equations 2 and 3 reduce to the standard nonlinear shallow water equations, which excludes dispersion. In the following, we will show results both with and without dispersion. Dispersive models are more realistic, but the effect of dispersion on tsunami amplitude and runup will be seen small near the coast where the wavelength of tsunami is large compared to ocean depth; the dispersive effect is most significant in deep ocean (i.e., the ratio of tsunami wavelength to ocean depth is small). Dispersion, however, affects tsunami waveforms even in the near-coast region.

A staggered-grid finite-difference method using nested grids was developed to solve Equations 1–3, following Baba et al. (2015). Without dispersion, the finite-difference method is fully explicit. To simulate dispersion, we use an iterative implicit solver by the method of successive over-relaxation (Young, 1971), a variant of the Gauss-Seidel method. A robust moving boundary scheme (e.g., Saito et al., 2014) was developed to track the instantaneous location of the coastline for accurate runup modeling. An absorbing boundary scheme (Cerjan, et al., 1985) with a sponge layer of 20 grid cells is used on the domain boundaries to avoid wave reflections.

The four grid layers used in this work are shown in Figure 1. The largest grid spacing is 1350 m, covering the majority of the computational domain. The grid spacing reduces to 450 m, 150 m, and 50 m successively (in a ratio of 3:1) as the coast is approached. Three overlapping regions in the 150 m grid and five overlapping regions in the 50 m grid are used to cover the Sanriku coast in high resolution. The smaller grid sizes near the coast are essential to resolve short tsunami wavelengths and model runup accurately. A two-way coupling between grid layers is implemented, which is described in detail in Baba et al. (2015). Communications are only allowed between two consecutive grid layers (e.g., between the 50 and 150 m grids), that is, there is no communication between different regions of the same grid layer (for example, the overlapping regions in the 50 m grid). The use of nested grids significantly reduces the degrees of freedom in the simulations. The bathymetry data provided by the Central Disaster Management Council of Government of Japan (Saito et al., 2014) are used for all the grid layers. All the simulations are run for 2 h with a time step of 0.625 s.

### 3. Initial Sea Surface Elevations From Three Models

To obtain the initial sea surface elevation for the 1896 Sanriku tsunami simulations, we rotate models I and II to follow the same fault strike as in model III ( $193^\circ$ ) and set the center of fault surface trace at ( $143.2^\circ\text{E}$ ,  $39.3^\circ\text{N}$ ), which is same as the northeast corner of the third subfault on the east side in model III (Figure 5d). The detailed locations of the subfaults in model III are given in Table 1 of Satake et al. (2017). The seafloor displacement in model III is calculated in a homogeneous half space following Okada (1985). In each model, we project the seafloor displacement onto the real bathymetry. We add the contributions of horizontal seafloor displacement due to local bathymetric slope to the vertical displacement to obtain the total seafloor



uplift (Tanioka & Satake, 1996). We then apply a lowpass filter (Kajiura, 1963) with a cutoff wavelength of 4 km (e.g., Saito et al., 2014) to obtain the initial sea surface elevation.

Figure 5 shows the initial sea surface elevations for the three models. The fault-perpendicular cross sections of horizontal and vertical seafloor displacements and initial sea surface elevations through the center of the fault are shown in Figure 6. The data for these three initial sea surface elevation profiles (Figure 5) are provided in the Supporting Information.

Model I has large horizontal seafloor displacement and a displacement discontinuity at the trench (blue line, Figure 6a) due to large shallow slip (Figure 3), while model II has negligible horizontal displacement and no discontinuity at the trench (red line, Figure 6a) because of diminishing trench slip caused by inelastic deformation (Figure 4). The small slip at shallow subfaults in model III produces modest horizontal displacement at the trench (green line, Figure 6a). Due to large localized buried slip (Figure 5d) model III produces a narrow seafloor uplift with a peak amplitude of 6.37 m (Figure 6b). The peak uplift in model II and I is 4.86 and 2.15 m, respectively (Figure 6b); the larger peak uplift in model II is due to inelastic wedge deformation (see Figures 3 and 4). The horizontal seafloor displacements contribute significantly to the sea surface elevation due to local bathymetric slope in all three models (Figure 6c). However, most of small-wavelength contributions shorter than ocean depth are filtered out by 3D response of the ocean (Kajiura, 1963). After the filtering, the large contribution from the horizontal displacement is mostly seen within 30 km from the trench in model I (blue solid line, Figure 6c). The narrow peak uplift of model III has also been significantly reduced by the filtering, while the peak uplift in model II is only modestly reduced due to the overall smooth nature of the inelastic seafloor deformation.

We compare the filtered profiles of initial sea surface elevation among three models (solid lines, Figure 6c). Model I has the longest wavelength among three models because the rupture breaks the entire width of the fault (~60 km; Figure 3). The initial elevation also has a broad and subdued peak (3.06 m). The large trench slip in this model is inefficient to produce sea surface elevation although the significant horizontal displacement contribution is included. The rupture of model II stops at about 10 km down dip from the trench due to inelastic wedge deformation (Figure 4), leading to a slightly smaller wavelength of the initial sea surface elevation. One significant difference from model I is a clear peak (4.35 m) about 20–25 km wide on top of a broad signal in model II, which is caused by inelastic wedge deformation. This small-wavelength feature is important to generate impulsive tsunamis, as will be shown below. The broad signal is controlled by the width of the rupture zone. The subsidence of these two models are quite similar. A sharp peak of about 25 km wide and 4.97 m high is seen in model III, which is due to 20 m buried slip on two 25 km wide subfaults (Figure 5d). Such large localized slip at shallow depths (3.5–7 km) generates a large narrow uplift, as well as a narrow subsidence nearly twice as large as that of models I and II, which is also clearly seen in the vertical seafloor displacement (Figure 6b). The elevation profile of model III is clearly narrower than that of model I and II. Although the uplift due to inelastic deformation is comparable in width in model II to that in model III the larger fault width (~50 km) leads to a larger dominant wavelength than model III. The along-strike extent of large uplift and subsidence in model III, also dominated by the two subfaults with localized slip, is about 100 km (Figure 5d). Models I and II have nearly uniform along-strike slip and inelastic deformation for about 200 km, extending from approximately 38.5°N to 40.2°N. We will see that these differences lead to different periods of tsunami signals and runup distributions on the Sanriku coast.

The efficiency of generating seafloor uplift in models II and III can be crudely compared as follows. The seafloor uplift in model III is mainly produced by 20 m localized buried slip on two subfaults (50 × 25 km each). The seismic potency on these two subfaults is  $2.5 \times 10^{10} \text{ m}^3$ . The seismic potency by inelastic deformation in the wedge in model II is  $2.13 \times 10^{10} \text{ m}^3$ , which accounts for most of the uplift. Ignoring the small differences in peak seafloor uplift and different rupture lengths both models require similar potency to produce similar seafloor uplift, implying similar efficiency.

However, there may be a plausibility issue in model III associated with unrealistically large stress change in the overlying wedge (e.g., Geist & Dmowska, 1999). The shear strain on the fault in this kinematic slip model can be crudely calculated by slip divided by the width of the subfault, which is equal to  $8.0 \times 10^{-4}$ . Assuming a shear modulus of 10–30 GPa for sedimentary rocks the stress drop on the two subfaults is 8–24 MPa on average. Dynamic stress changes off the fault can be an order of magnitude or more larger than this

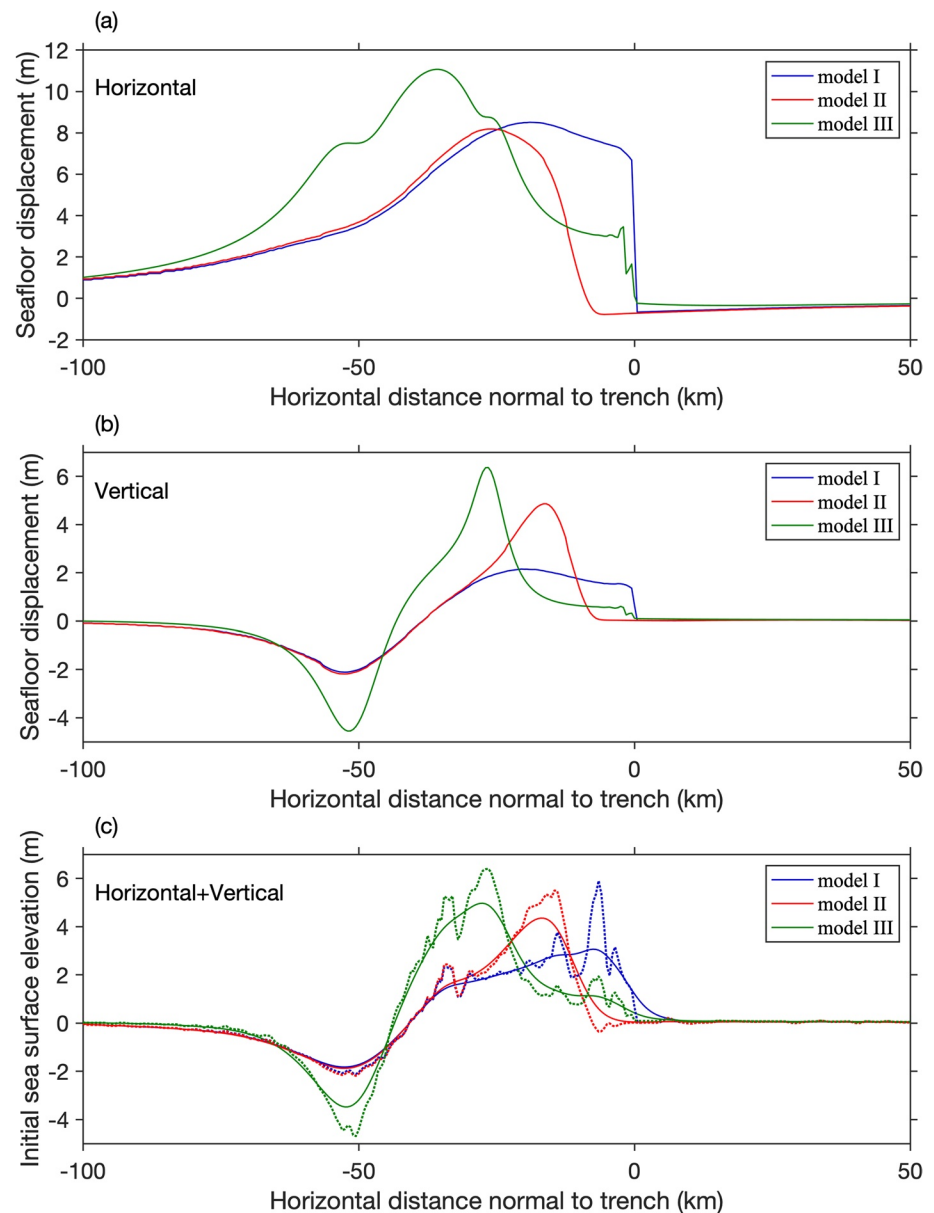


**Figure 6.** Comparisons of (a) horizontal seafloor displacements, (b) vertical seafloor displacements, and (c) initial sea surface elevations at a cross section shown in Figure 5. The contribution of horizontal seafloor displacement is included in the calculation of initial sea surface elevation in (c). The unfiltered initial sea surface elevations (dotted lines) contain many small-wavelength variations, which cannot exist due to the 3D ocean response. The solid lines show the initial sea surface elevation after applying a Kajiura lowpass filter with a cutoff wavelength of 4 km. The horizontal seafloor displacement contributes significantly to initial sea surface elevation in model I (within 30 km from the trench), but not in the other two models.

static estimate (e.g., Andrews, 2005). There are also stress singularities at the edges of subfaults due to slip discontinuities. The depth of slip is shallow ( $\sim 3.5\text{--}7$  km), which is essential to generate large uplift in this model. Due to low confining pressure, possible fluid overpressure, and weak sediments in the wedge such large stress changes may cause wedge failure leading to inelastic deformation, similar to model II. Thus, despite generating short-wavelength seafloor uplift efficiently large localized buried slip on shallow narrow subfaults may be mechanically implausible. This issue may need further investigations.

#### 4. Results

We show the snapshots of tsunami due to model II when wave dispersion is included (Figure 7). As the tsunami propagates toward the coast tsunami speed decreases due to decreasing ocean depth. Clear narrowing of wavelength and increase of wave amplitude is seen, which is the well-known shoaling effect. Small dispersive signals can be seen after the leading tsunami due to the small wavelength of uplift relative to ocean depth in the model. Such narrow-wavelength leading tsunami will be manifested as impulsive signals in time histories, to be shown below. Shortly after 30 min tsunami starts to impact the Sanriku coast with large wave amplitude. The direct impact of the leading impulsive tsunami produces the largest runup in the model. Edge waves as energy trapped near the shore last long after the leading tsunami hits the coast. Tsunami propagating into deep ocean shows the opposite effect. The increase of ocean depth increases wave speed and tsunami wavelength and decreases the wave amplitude. Strong wave dispersion is evident. The dispersion in deep ocean due to long travel distance has been shown by several studies (e.g., Baba et al., 2015; Horrillo et al., 2006; Saito et al., 2014; Tanioka et al., 2018). Here the strong dispersion is largely due to the small wavelength of seafloor uplift relative to ocean depth.

The wavefield without dispersion for model II is much simpler (Figure S1). The leading tsunami toward the coast is similar to Figure 7 although stronger shoaling effects can be seen. The increase of wave amplitude and narrowing of leading tsunami are slightly more significant. The wave amplitude in deep ocean is significantly higher than that with dispersion. The snapshots of wavefield with and without dispersion for models I and III (Figures S2–S5) show similar patterns.

The waveforms with and without dispersion at five offshore stations (TM1, TM2, and Iwate N, M, and S) and one Deep-ocean Assessment and Reporting of Tsunami (DART) station (21418) are shown in Figure 8. The data recorded in the 2011 Tohoku earthquake at these stations (Figure 2) are high-pass filtered at 15 min to take out the impulsive signal by removing the long-period components caused by the broad seafloor uplift south of 39°N, shown as a reference. We do not aim to fit the 2011 data in this work as the simulations are for the 1896 Sanriku tsunami. Our focus here is more on the amplitude and wavelength of seafloor uplift necessary to generate the signal similar to the impulsive signal observed in 2011. The timing of the filtered data (shown in black) is with respect to the origin time of the 2011 Tohoku earthquake, which gives rise to the apparent waveform shifts in the figure. At five nearshore stations a clear impulsive signal of the leading tsunami is seen, which is not significantly affected by the dispersion. The impulsive signal without dispersion is slightly larger and narrower than the dispersive signal because dispersion tends to smooth out the wavefield. Both nondispersive and dispersive impulsive signals show a remarkable similarity to the impulsive signals observed in the 2011 Tohoku tsunami in terms of impulse width and amplitude, which is due to the small wavelength of seafloor uplift in model II. The observed signals in 2011 show slightly narrower width, suggesting that the wavelength of model II needs to be reduced if the 2011 data is to be fitted, which can be achieved by narrowing the fault width. The smaller amplitude of the data at Iwate N indicates that rupture extent of the 2011 Tohoku earthquake may not reach as far north as in model II or the seafloor uplift in the north was smaller than in model II. At DART 21418, the observed signal shows clear wave dispersion, which is well reproduced by the dispersive model, as shown by previous studies (e.g., Baba et al., 2015; Saito et al., 2014; Tappin et al., 2014). The nondispersive model oversimplifies the waveform and significantly overestimates the tsunami amplitude in deep ocean. Waveform comparisons with and without dispersion for models I and III are shown in Figures S6 and S7, displaying similar patterns.

We compare the waveforms at all stations for the three dispersive models (Figure 9). The width of the impulsive signal in model I is the largest among three models because model I has the longest wavelength of initial sea surface elevation (Figures 5 and 6). The initial sea surface elevation in model I is the smallest of the three models, resulting in that model having the smallest amplitude of the impulsive signal at four of five offshore stations. At Iwate N, the impulsive signal of Model III is the smallest because this model has a shorter rupture extent (see Figure 5c). Model II produces more impulsive signal and larger wave amplitude than model I at all stations due to the smaller wavelength and larger total seafloor uplift. The most impulsive signal is seen in model III, which has the shortest wavelength due to large localized buried slip on 25 km wide subfaults, but may be mechanically implausible as mentioned earlier. This model also generates the largest tsunami height at four of five offshore stations due to larger seafloor uplift and a smaller rupture extent (Figure 5c). The waveform comparison for three nondispersive models (Figure S8) shows

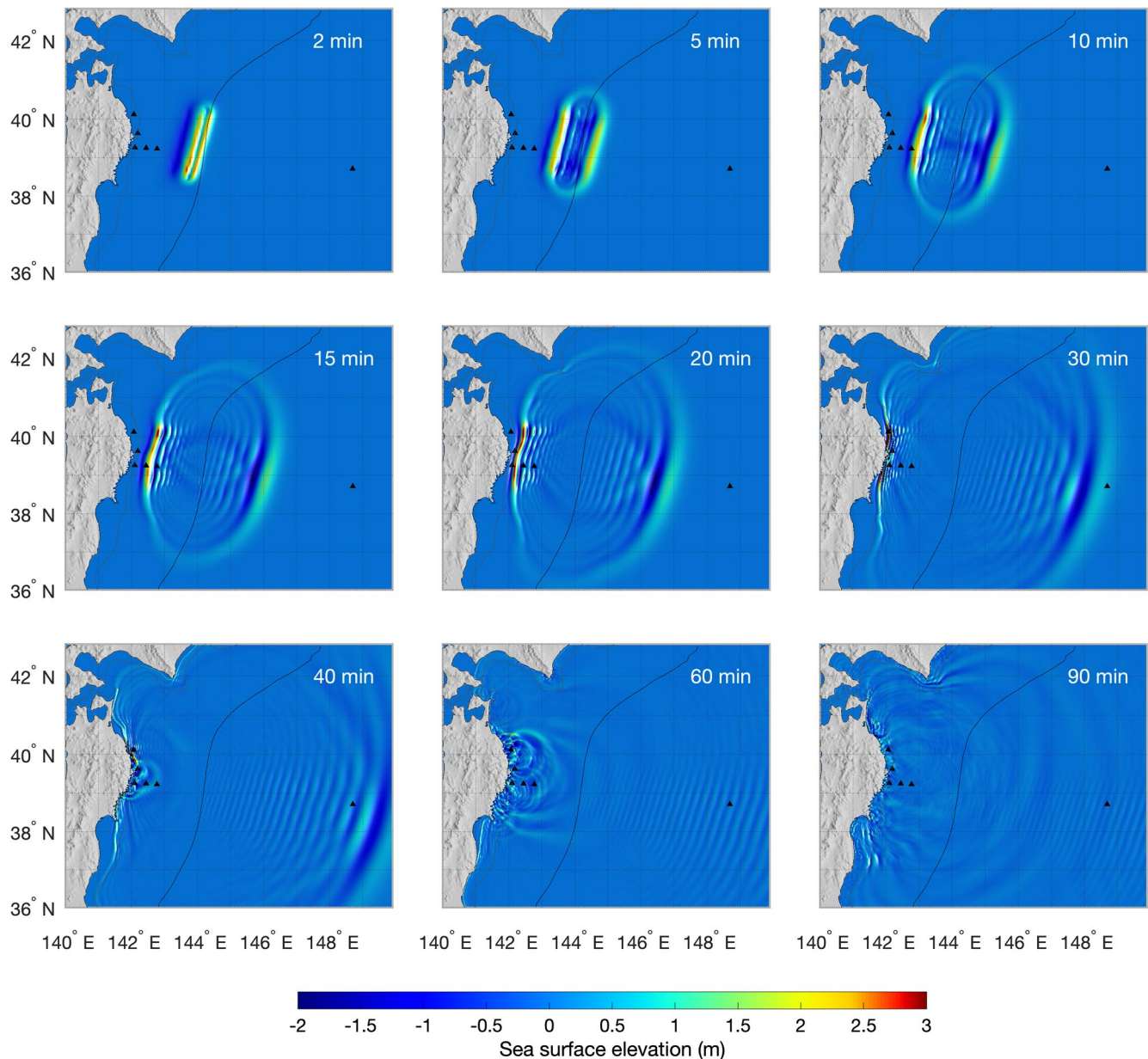


**Figure 7.** Snapshots of sea surface elevation for model II with dispersion. Clear wave shoaling effect is seen on the landward tsunami, with increasing amplitude and decreasing wavelength as tsunami slows down. The tsunami recorded at five stations (shown by black triangles) off the Sanriku coast with impulsive signals are shown in Figure 8. Seaward tsunami shows strong wave dispersion largely due to small wavelength of seafloor uplift relative to ocean depth, which is recorded at DART 21418.

slightly narrower impulsive signals than the dispersive results, consistent with Figures 8, S6, and S7, and the patterns among three models are similar.

The maximum tsunami heights of three dispersive models are illustrated in Figure 10. Model II produces overall larger tsunami heights than model I, which is consistent with the waveforms shown in Figure 9. Model III has the largest tsunami height between about 39°N and slightly south of 40°N because the initial sea surface elevation is concentrated above the two-central subfaults with large localized buried slip. Clear focusing of wave energy is seen, generating large tsunami heights on the Sanriku coast south of 40°N. This model, however, generates smaller tsunami height north of 40°N due to its shorter along-strike extent of seafloor uplift than models I and II (see also the waveform at Iwate N in Figure 9). The maximum tsunami



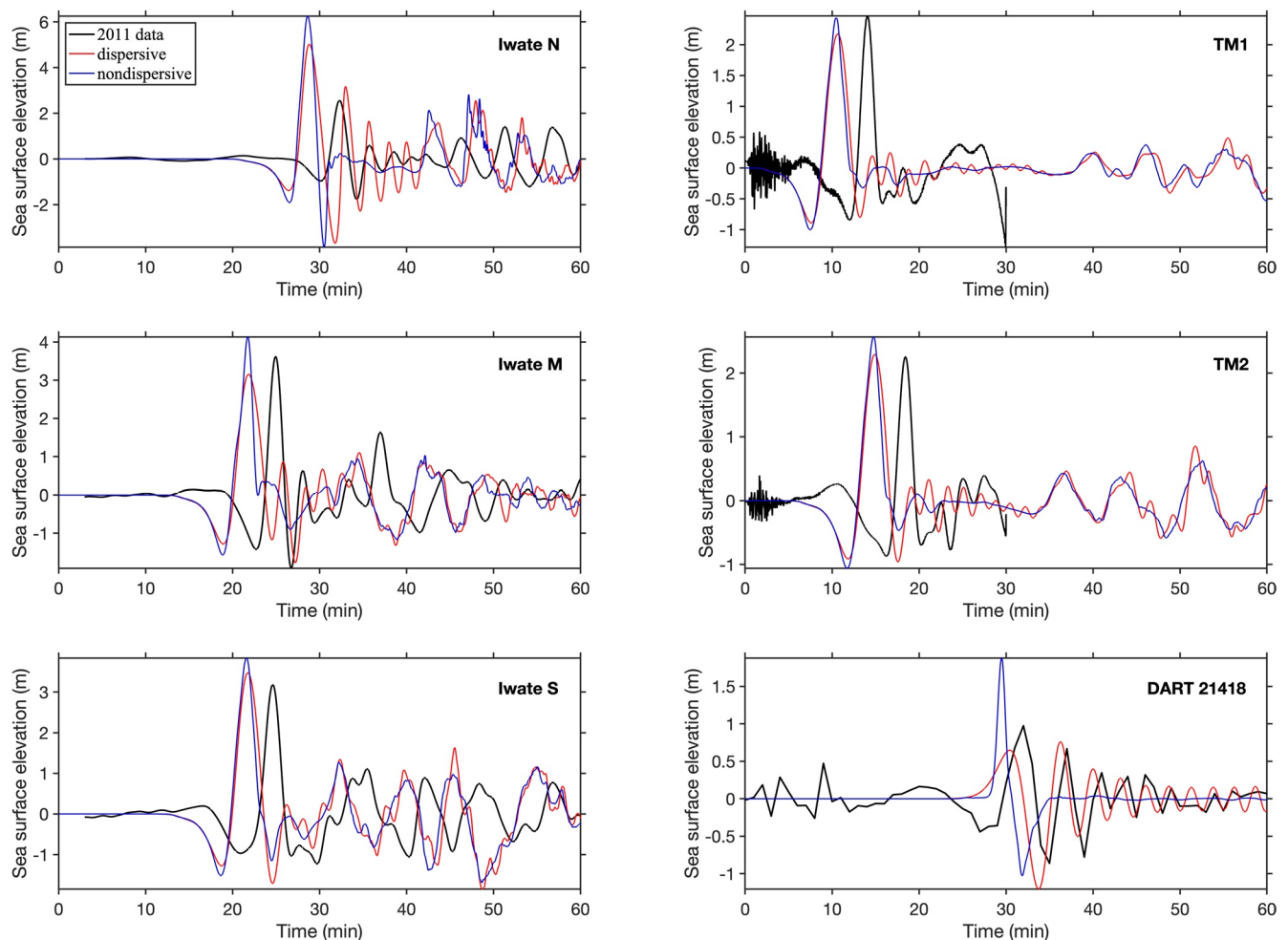


**Figure 8.** Comparison of simulated waveforms at six stations with (red) and without (blue) dispersion for model II. The observed data (Figure 2) high-pass filtered with a 15-min cutoff period are shown in black for reference. We do not intend to match the 2011 data because the simulations are for the 1896 Sanriku tsunami. The 2011 data are plotted with respect to the origin time of the 2011 Tohoku earthquake, which gives rise to the apparent waveform shifts. Both nondispersive and dispersive waveforms show a clear impulsive signal, similar to the observed signal in 2011. Dispersion effects for the five offshore stations are minor. The dispersive impulsive signal is slightly wider, smaller, and smoother than the nondispersive signal. At DART 21418 the nondispersive waveform is significantly oversimplified.

height for the three nondispersive models (Figure S9) show similar patterns landward with slightly larger amplitudes than the dispersive models. The peak tsunami amplitude in deep ocean is significantly overestimated and unrealistic due to the exclusion of dispersion.

Finally, tsunami runup along the Sanriku coast for the three models without and with dispersion are shown in Figures 11 and 12, respectively. All the simulated runup values in the three models are shown. In order to compare the three models clearly, the runup values are shaded and outlined by a peak envelope function in each model, which is obtained by spline interpolation of local maxima over 20 points. The runup data of the 1896 Sanriku tsunami collected at 144 sites by Iki (1897) and 266 sites by Matsuo (1933) are also shown. The root-mean-square (RMS) of runup heights at all locations in the three models with and without dispersion are listed in Table 1. The table also lists the RMS of the ratios of simulated to observed runup heights at the observation sites of Iki (1897) and Matsuo (1933). The data at which the simulated runup does not exist (i.e., simulated tsunami does not reach the observation point) is not included in the calculation. The comparison of simulated runup (with and without dispersion) with data in each model is detailed in Figures S10–S12.

Nondispersive models in general generate slightly larger runup than dispersive models with a possible exception of Model III (see also Figures S10–S12), consistent with distributions of maximum tsunami height

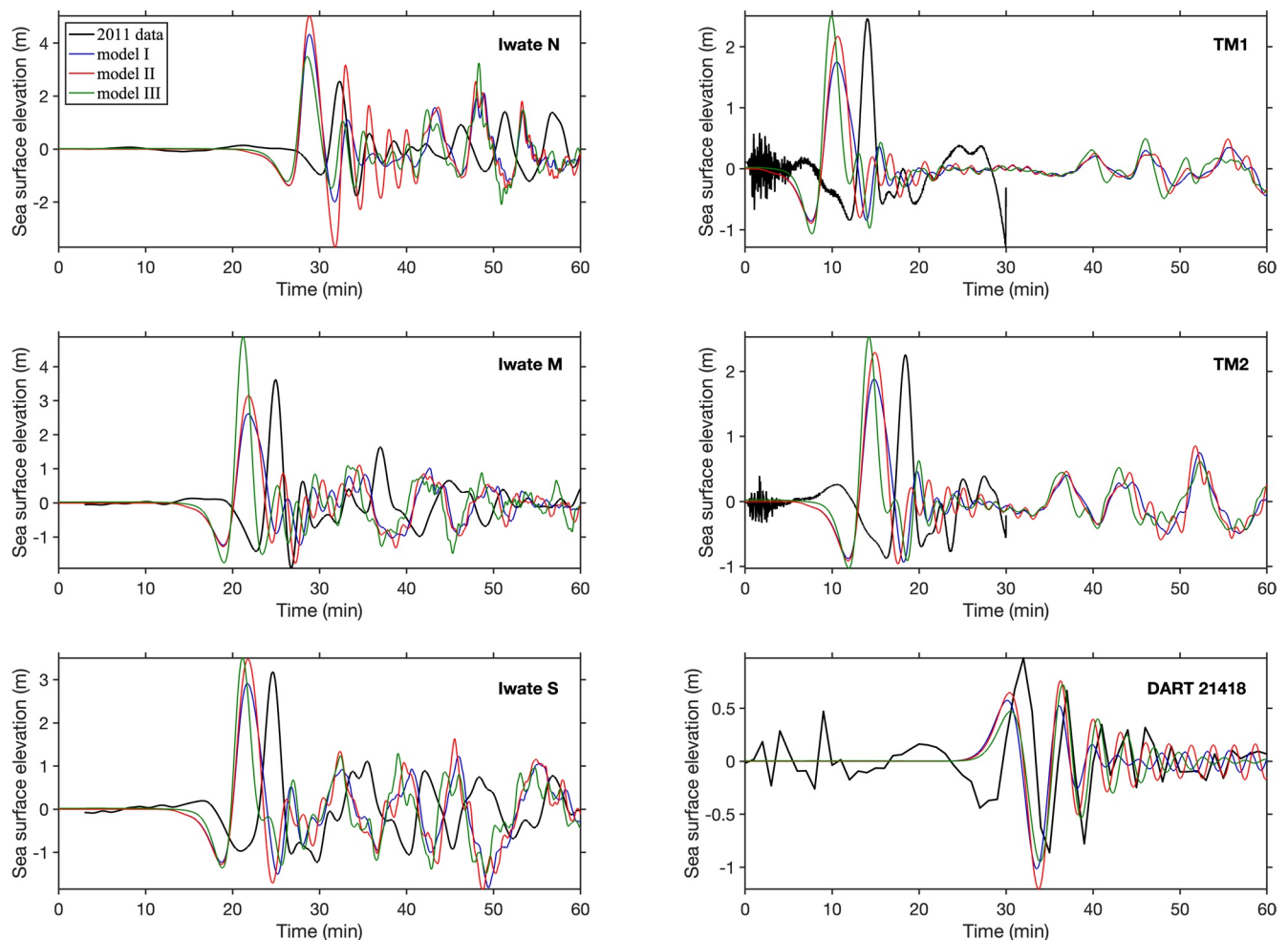


**Figure 9.** Comparison of simulated waveforms from three dispersive models. Model I produces the smallest and widest impulse at four of five offshore stations due to its smallest and longest-wavelength initial sea surface elevation (Figure 6). Model III produces the smallest amplitude at Iwate N because of its shorter along-strike extent of seafloor uplift (Figure 5). The impulsive signal in Model II is consistently larger and narrower than model I. Model III produces the narrowest impulse due to its shortest wavelength among three models, however, it may contain mechanical inconsistencies at the earthquake source region.

(Figures 10 and S9). The differences in the runup of model III with and without dispersion appear indistinguishably small. Model II produces consistently larger runup than model I although the two runup patterns are similar, which can also be seen in the RMS of simulated runup (Table 1). The difference in runup between these two models can be well above 5 m (Figures 11d–11f and 12d–12f) although the difference in the initial sea surface elevations is slightly above 1 m, illustrating the stronger shoaling effect and the amplification of small-wavelength tsunami by the bathymetry and coastal topography of the Sanriku coast.

The runup of model II show a remarkable similarity to the 1896 runup data, especially in the overall trend of runup distribution. The largest tsunami runup observed in the 1896 Sanriku tsunami, 38.2 m in Ryori-Shirohama (141.8071°E, 39.0569°N), is nearly reproduced by both the nondispersive and dispersive models with a slightly better match in the nondispersive model. The RMS of the ratios of simulated to observed runup heights is 1.04 (without dispersion) and 1.01 (with dispersion), better than the other two models. These remarkable fits are obtained without any tuning of the model.

Model III significantly overestimates the runup height between about 39.3°N and 39.9°N, which is about the same region with large peak tsunami height in Figure 10. The model underestimates the runup elsewhere, including the large runup in Ryori-Shirohama, due to its shorter along-strike extent of seafloor uplift, which results in the RMS of the ratios of simulated to observed runup less than 1.0 in this model.

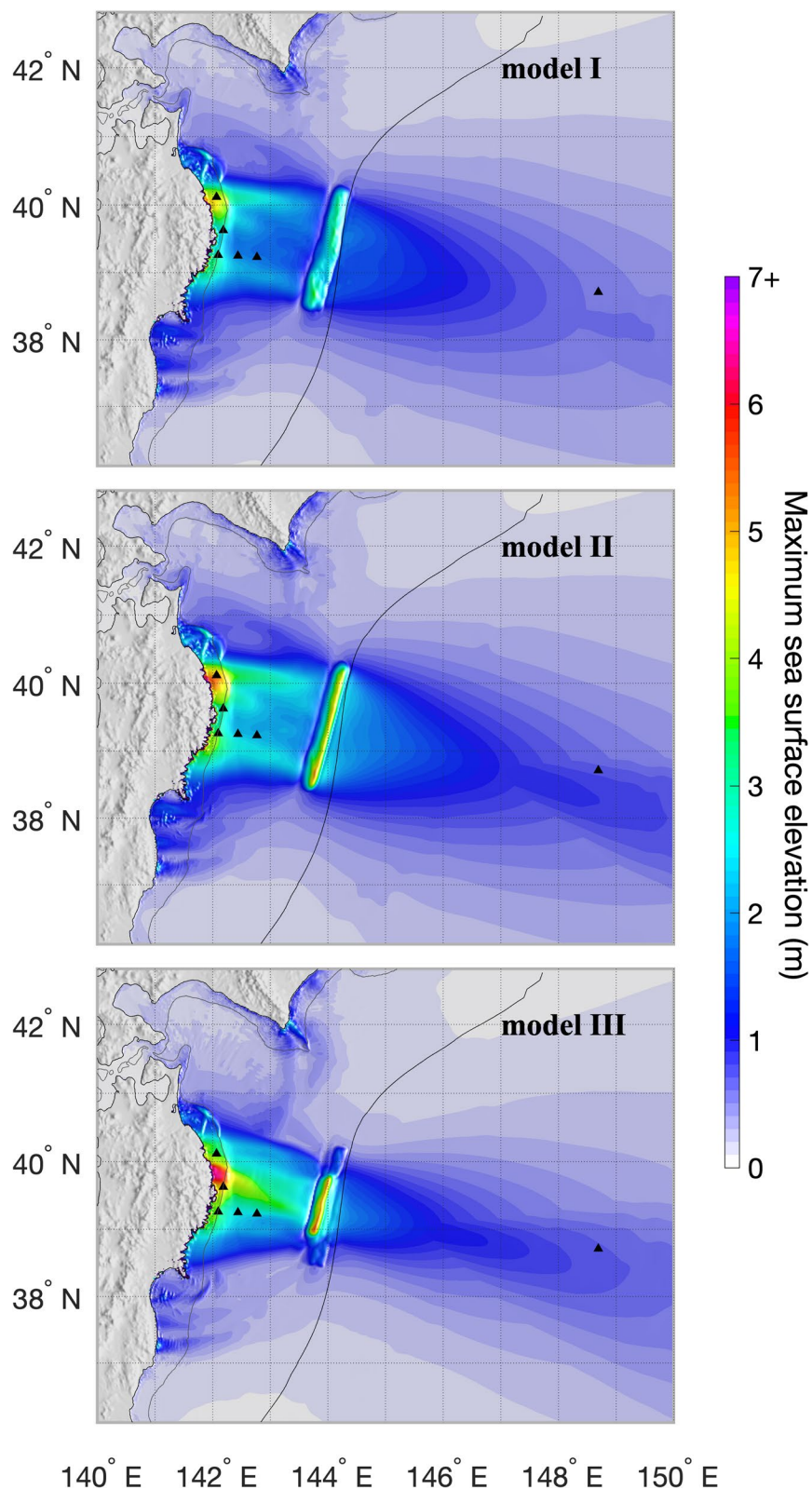


**Figure 10.** Comparison of maximum sea surface elevation for three dispersive models. Model II generates consistently larger tsunami height than model I. The localized slip and uplift of model III produce large tsunami height between about 39°N and 40°N. The black line shows the trench. The 200 m depth contour by a thin gray line shows approximately the width of continental shelf.



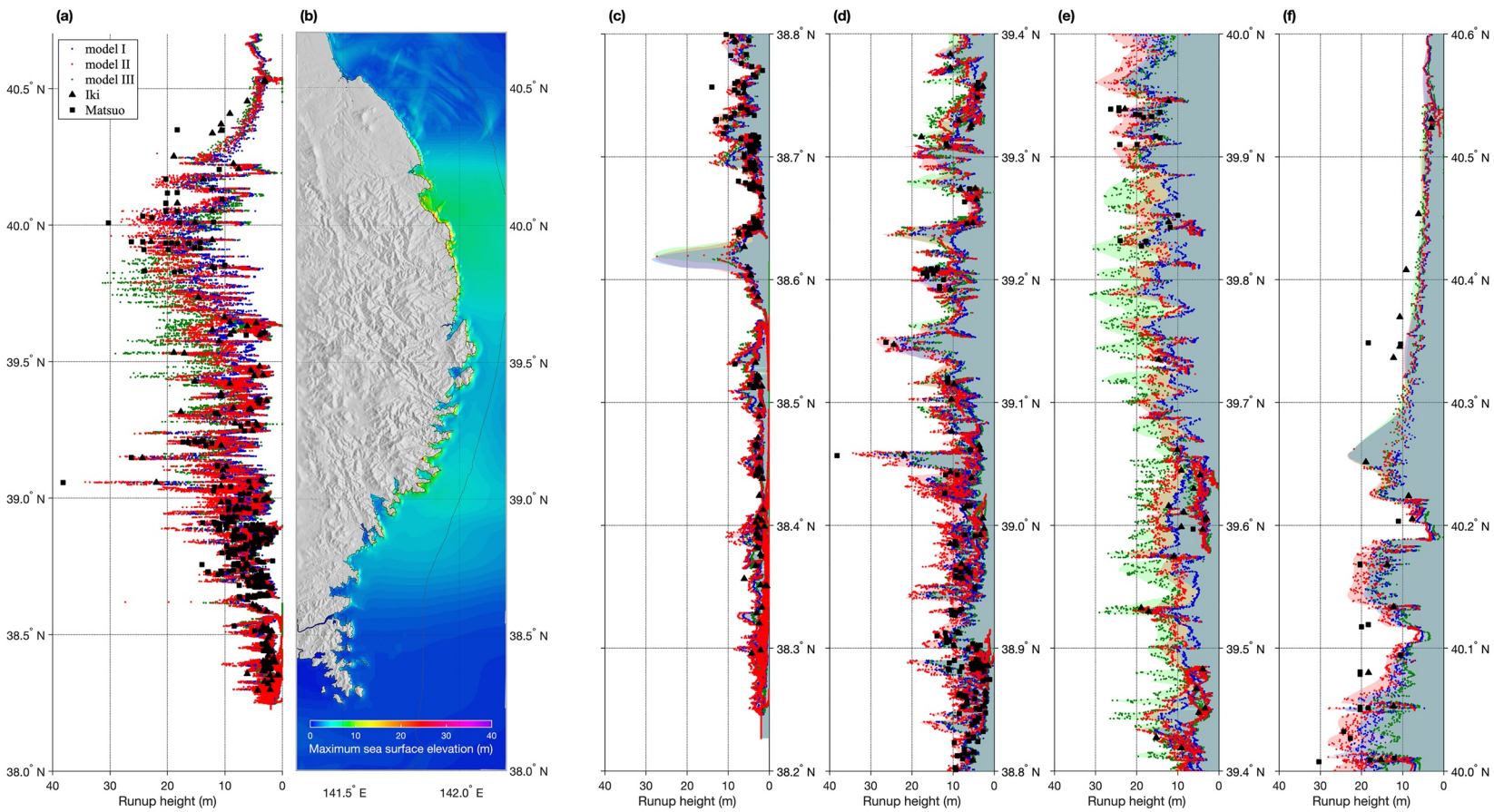


**Figure 11.** Comparison of runup from three nondispersive models of the 1896 Sanriku tsunami. (a) All the runup values along the coast calculated from three models compared with the data of Iki (1897) and Matsuo (1933), (b) map of the Sanriku coast with the maximum sea elevation of model II, (c–f) enlarged view of comparison in (a) on four segments with a shaded region outlined by an envelope function for each model. Each envelope function is determined using spline interpolation over local maxima separated by 20 points. A remarkable similarity between the runup of model II and data can be seen. Model II produces consistently larger runup than model I. Model III overestimates the runup between about 39.3°N and 39.9°N and underestimates the runup elsewhere.



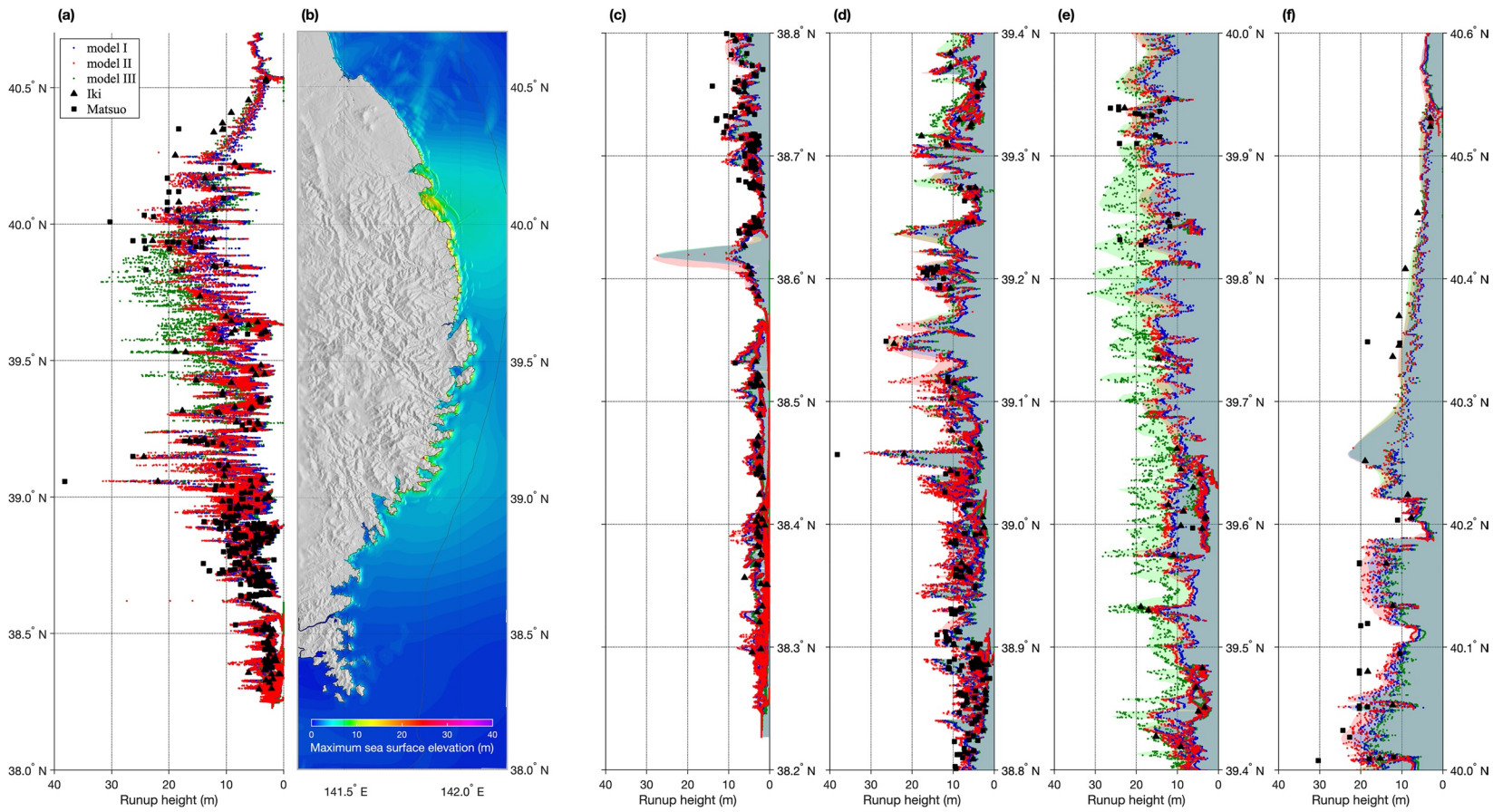


**Figure 12.** Similar to Figure 11, but for three dispersive models. The modeled runup are slightly smaller than in Figure 10. Similar patterns among three models can be seen.

**Table 1**  
*The Root-Mean-Square (RMS) of Simulated Runup at all Locations in the Models and Ratios of Simulated to Observed Runup at the Observation Sites*

		RMS of simulated runup (m)	RMS of ratios of simulated to observed runup
Model I	Nondispersive	6.71	0.92
	Dispersive	6.56	0.91
Model II	Nondispersive	8.23	1.04
	Dispersive	7.60	1.01
Model III	Nondispersive	7.42	0.84
	Dispersive	7.50	0.85

## 5. Discussion and Conclusions

We have presented three models of the 1896 Sanriku tsunami by using two dynamic rupture models (Ma & Nie, 2019) and one kinematic slip model (Satake et al., 2017) of the 1896 Sanriku earthquake. The short-wavelength seafloor uplift is shown to be instrumental in generating impulsive tsunami, which can be greatly amplified by the rugged coast of Sanriku to produce large runup. We show that the inelastic wedge deformation model (Model II), with width of seafloor uplift about 20–25 km, produces impulsive tsunami similar to what was observed at two ocean-bottom pressure sensors (TM1 and TM2) and three GPS wave gauges (Iwate N, M, and S) offshore the Sanriku coast in the 2011 Tohoku tsunami. Our focus in this work is not to fit the 2011 tsunami data as the simulations are for the 1896 Sanriku tsunami, but to show a physical mechanism capable of generating such short-wavelength seafloor uplift and impulsive tsunami.

Despite the fact that Model III (a kinematic slip model with elastic dislocation) can also generate short-wavelength seafloor uplift efficiently this model may be mechanically implausible; the large stress changes in the overriding wedge can likely cause failure leading to inelastic deformation, similar to model II. The physical plausibility of model III may need further investigations. Large trench slip with mostly elastic wedge deformation (model I) produces broader and smaller seafloor uplift largely due to the shallow dipping fault geometry, giving rise to smaller and longer-period tsunami than the other two models.

Inelastic wedge deformation (model II) produces consistently larger tsunami heights than large shallow slip (model I), because the former model produces larger seafloor uplift and shorter wavelength than does the latter. The difference in runup between these two models can be more than five times the difference in the initial sea surface elevations due to the acute sensitivity of runup to short tsunami wavelengths and stronger shoaling effect of short-period tsunami. This model also produces runup on the Sanriku coast with a remarkable similarity to the observed runup of the 1896 Sanriku tsunami without any tuning of the model.

The 1896 Sanriku earthquake is a tsunami earthquake (Kanamori, 1972), which caused weak high-frequency seismic radiation and large tsunami. Inelastic wedge deformation is a large energy sink and generates seafloor uplift efficiently, which can explain both the characteristics of tsunami earthquakes (Ma, 2012; Ma & Hirakawa, 2013). In this work, we extend the models of Ma and Nie (2019) and further show that short-wavelength inelastic seafloor uplift can produce impulsive tsunami to be amplified on the Sanriku coast, resulting in large runup. Thus, inelastic wedge deformation is a possible mechanism that can account for nearly all the important characteristics of the 1896 Sanriku earthquake. Fully coupled models of dynamic rupture and tsunami (e.g., Lotto et al., 2018; Wilson & Ma, 2021) for the 1896 Sanriku earthquake should be done next to more rigorously model tsunami excitation and explore the radiation characteristics of seismic and ocean acoustic waves due to inelastic deformation, which can provide important insights to tsunami early warning in the Japan Trench margin.

No large shallow slip near the trench or large submarine landslide were observed north of 39°N in the 2011 Tohoku earthquake (Fujiwara et al., 2017). Given the similarity of tsunami runup generated by the 1896 Sanriku and 2011 Tohoku earthquakes and the capability of inelastic wedge deformation in generating impulsive tsunami, large tsunami runup, and deficient high-frequency seismic radiation we suggest, as an alternative to shallow-slip models, that the devastating 2011 Tohoku tsunami on the Sanriku coast may be caused by inelastic wedge deformation north of 38.5°N due to the presence of thick sediments (e.g., Kodaira et al., 2017; Tsuru et al., 2002).

## Data Availability Statement

The bathymetry data provided by the Central Disaster Management Council of Government of Japan is available at <https://www.geospatial.jp/ckan/dataset/1976> (in Japanese). The recorded data at three GPS wave gauges (Iwate N, M, and S) in the 2011 Tohoku tsunami were downloaded from <https://nowphas.mlit>.

[go.jp/pastdatars/data/NOWPHAS\\_Tsunami\\_data.zip](https://go.jp/pastdatars/data/NOWPHAS_Tsunami_data.zip). The ocean bottom pressure gauge data off the Sanriku coast (TM1 and TM2) was provided by the Earthquake Research Institute of the University of Tokyo. The DART 21418 data was downloaded from [https://www.ngdc.noaa.gov/hazard/dart/2011honshu\\_dart.html](https://www.ngdc.noaa.gov/hazard/dart/2011honshu_dart.html). The data on which this article is based are available in Ma and Nie (2019) and Satake et al. (2017).

## Acknowledgments

The authors thank an anonymous reviewer, Iris van Zelst, and Alice Gabriel (Associate Editor) for their thoughtful and constructive comments. Comments from Steve Day improved the clarity of the paper. This work is supported by the National Science Foundation (award no. EAR-1620201).

## References

- Abe, K. (1978). A dislocation model of the 1933 Sanriku earthquake consistent with the tsunami waves. *Journal of Physics of the Earth*, 26(4), 381–396. <https://doi.org/10.4294/jpe1952.26.381>
- Andrews, D. J. (2005). Rupture dynamics with energy loss outside the slip zone. *Journal of Geophysical Research*, 110(B1), B01307. <https://doi.org/10.1029/2004jb003191>
- Baba, T., Takahashi, N., Kaneda, Y., Ando, K., Matsuoka, D., & Kato, T. (2015). Parallel implementation of dispersive tsunami wave modeling with a nesting algorithm for the 2011 Tohoku Tsunami. *Pure and Applied Geophysics*, 172(12), 3455–3472. <https://doi.org/10.1007/s00024-015-1049-2>
- Cerjan, C., Kosloff, D., Kosloff, R., & Reshef, M. (1985). A nonreflecting boundary condition for discrete acoustic and elastic equations. *Geophysics*, 50, 705–708. <https://doi.org/10.1190/1.1441945>
- Dresback, K. M., Kolar, R. L., & Dietrich, J. C. (2005). On the form of the momentum equation for shallow water models based on the generalized wave continuity equation. *Advances in Water Resources*, 28(4), 345–358. <https://doi.org/10.1016/j.advwatres.2004.11.011>
- Fujiwara, T., Dos Santos Ferreira, C., Bachmann, A. K., Strasser, M., Wefer, G., Sun, T., et al. (2017). Seafloor displacement after the 2011 Tohoku-oki earthquake in the Northern Japan trench examined by Repeated Bathymetric surveys. *Geophysical Research Letters*, 44(23), 11833–11839. <https://doi.org/10.1002/2017gl075839>
- Fujiwara, T., Kodaira, S., No, T., Kaiho, Y., Takahashi, N., & Kaneda, Y. (2011). The 2011 Tohoku-oki earthquake: Displacement reaching the trench axis. *Science*, 334(6060), 1240. <https://doi.org/10.1126/science.1211554>
- Geist, E. L., & Dmowska, R. (1999). Local tsunamis and distributed slip at the source. *Pure and Applied Geophysics*, 154, 485–512. <https://doi.org/10.1007/s000240050241>
- Horrillo, J., Kowalik, Z., & Shigihara, Y. (2006). Wave dispersion study in the Indian Ocean-Tsunami of December 26, 2004. *Marine Geodesy*, 29(3), 149–166. <https://doi.org/10.1080/01490410600939140>
- Hossen, M. J., Cummins, P. R., Dettmer, J., & Baba, T. (2015). Tsunami waveform inversion for sea surface Displacement following the 2011 Tohoku earthquake: Importance of dispersion and source kinematics. *Journal of Geophysical Research: Solid Earth*, 120(9), 6452–6473. <https://doi.org/10.1002/2015jb011942>
- Iki, T. (1897). Field survey report of the 1896 Sanriku tsunami. *Rep Imp Earthq Invest Comm*, 11, 5–34. (in Japanese).
- Kajiura, K. (1963). Leading wave of a tsunami. *Bulletin of the Earthquake Research Institute*, 43, 535–571. <https://doi.org/10.1086/dia41504341>
- Kanamori, H. (1971). Seismological evidence for a lithospheric normal faulting—The Sanriku earthquake of 1933. *Physics of the Earth and Planetary Interiors*, 4(4), 289–300. [https://doi.org/10.1016/0031-9201\(71\)90013-6](https://doi.org/10.1016/0031-9201(71)90013-6)
- Kanamori, H. (1972). Mechanism of tsunami earthquakes. *Physics of the Earth and Planetary Interiors*, 6(5), 346–359. [https://doi.org/10.1016/0031-9201\(72\)90058-1](https://doi.org/10.1016/0031-9201(72)90058-1)
- Kirby, J. T., Shi, F., Tehranirad, B., Harris, J. C., & Grilli, S. T. (2013). Dispersive tsunami waves in the ocean: Model equations and sensitivity to dispersion and Coriolis effects. *Ocean Modelling*, 62, 39–55. <https://doi.org/10.1016/j.ocemod.2012.11.009>
- Kodaira, S., Fujiwara, T., Fujie, G., Nakamura, Y., & Kanamatsu, T. (2020). Large coseismic slip to the trench during the 2011 Tohoku-Oki Earthquake. *Annual Review of Earth and Planetary Sciences*, 48(1), 321–343. <https://doi.org/10.1146/annurev-earth-071719-055216>
- Kodaira, S., Linuma, T., & Imai, K. (2021). Investigating a tsunamigenic megathrust earthquake in the Japan Trench. *Science*, 371, eabe1169. <https://doi.org/10.1126/science.abe1169>
- Kodaira, S., Nakamura, Y., Yamamoto, Y., Obana, K., Fujie, G., No, T., et al. (2017). Depth-varying structural characters in the rupture zone of the 2011 Tohoku-oki earthquake. *Geosphere*, 13(5), 1408–1424. <https://doi.org/10.1130/ges01489.1>
- Lay, T. (2018). A review of the rupture characteristics of the 2011 Tohoku-oki MW 9.1 earthquake. *Tectonophysics*, 733, 4–36. <https://doi.org/10.1016/j.tecto.2017.09.022>
- Lay, T., Kanamori, H., Ammon, C. J., Koper, K. D., Hutko, A. R., Ye, L., et al. (2012). Depth-varying rupture properties of subduction zone megathrust faults. *Journal of Geophysical Research*, 117(B4), B04311. <https://doi.org/10.1029/2011jb009133>
- Lotto, G. C., Jeppson, T. N., & Dunham, E. M. (2018). Fully coupled simulations of megathrust earthquakes and tsunamis in the Japan Trench, Nankai trough, and Cascadia subduction zone. *Pure and Applied Geophysics*, 176(9), 4009–4041. <https://doi.org/10.1007/s00024-018-1990-y>
- Ma, S. (2012). A self-consistent mechanism for slow dynamic deformation and tsunami generation for earthquakes in the shallow subduction zone. *Geophysical Research Letters*, 39(11), L11310. <https://doi.org/10.1029/2012gl051854>
- Ma, S., & Hirakawa, E. T. (2013). Dynamic wedge failure reveals anomalous energy radiation of shallow subduction earthquakes. *Earth and Planetary Science Letters*, 375, 113–122. <https://doi.org/10.1016/j.epsl.2013.05.016>
- Ma, S., & Nie, S. (2019). Dynamic wedge failure and along-arc variations of tsunamigenesis in the Japan Trench margin. *Geophysical Research Letters*, 46(15), 8782–8790. <https://doi.org/10.1029/2019gl083148>
- Maeda, T., Furumura, T., Sakai, S., & Shinohara, M. (2011). Significant tsunami observed at Ocean-bottom pressure gauges during the 2011 off the Pacific coast of Tohoku earthquake. *Earth Planets and Space*, 63(7), 803–808. <https://doi.org/10.5047/eps.2011.06.005>
- Matsuo, H. (1933). Report on the survey of the 1933 Sanriku tsunami. *Report of the Civil Engineering Laboratory*, 24, 83–136. (in Japanese).
- Mori, N., Takahashi, T., Yasuda, T., & Yanagisawa, H. (2011). Survey of 2011 Tohoku earthquake Tsunami inundation and run-up. *Geophysical Research Letters*, 38(7), L00G14. <https://doi.org/10.1029/2011gl049210>
- Okada, Y. (1985). Surface deformation due to shear and tensile faults in a half-space. *Bulletin of the Seismological Society of America*, 75, 1135–1154. [https://doi.org/10.1016/0148-9062\(86\)90674-1](https://doi.org/10.1016/0148-9062(86)90674-1)
- Roeber, V., Cheung, K. F., & Kobayashi, M. H. (2010). Shock-capturing Boussinesq-type model for nearshore wave processes. *Coastal Engineering*, 57(4), 407–423. <https://doi.org/10.1016/j.coastaleng.2009.11.007>
- Rogers, S. R., & Mei, C. C. (1978). Nonlinear resonant excitation of a long and narrow bay. *Journal of Fluid Mechanics*, 88, 161–180. <https://doi.org/10.1017/s0022112078002037>

- Saito, T. (2019). *Tsunami generation and propagation*. Springer. <https://doi.org/10.1007/978-4-431-56850-6>
- Saito, T., Inazu, D., Miyoshi, T., & Hino, R. (2014). Dispersion and nonlinear effects in the 2011 Tohoku-Oki earthquake tsunami. *Journal of Geophysical Research: Oceans*, 119(8), 5160–5180. <https://doi.org/10.1002/2014jc009971>
- Satake, K., Fujii, Y., Harada, T., & Namegaya, Y. (2013). Time and space distribution of coseismic slip of the 2011 Tohoku earthquake as inferred from tsunami waveform data. *Bulletin of the Seismological Society of America*, 103(2B), 1473–1492. <https://doi.org/10.1785/0120120122>
- Satake, K., Fujii, Y., & Yamaki, S. (2017). Different depths of near-trench slips of the 1896 Sanriku and 2011 Tohoku earthquakes. *Geoscience Letters*, 4(1). <https://doi.org/10.1186/s40562-017-0099-y>
- Shimozono, T., Cui, H., Pietrzak, J. D., Fritz, H. M., Okayasu, A., & Hooper, A. J. (2014). Short wave amplification and extreme runup by the 2011 Tohoku Tsunami. *Pure and Applied Geophysics*, 171(12), 3217–3228. <https://doi.org/10.1007/s00024-014-0803-1>
- Shimozono, T., Sato, S., Okayasu, A., Tajima, Y., Fritz, H. M., Liu, H., & Takagawa, T. (2012). Propagation and Inundation characteristics of the 2011 Tohoku tsunami on the Central Sanriku Coast. *Coastal Engineering Journal*, 54(1). <https://doi.org/10.1142/s0578563412500040>
- Shuto, N., Imamura, F., Koshimura, S., Satake, K., & Matsutomi, H. (2007). *Encyclopedia of tsunamis (tsunami no jiten)* (p. 350). Tokyo: Asakura Publishing.
- Tanioka, Y., Ramirez, A. G., & Yamanaka, Y. (2018). Simulation of a dispersive tsunami due to the 2016 El Salvador–Nicaragua outer-rise earthquake ( $M_w$  6.9). *Pure and Applied Geophysics*, 175(4), 1363–1370. <https://doi.org/10.1007/s00024-018-1773-5>
- Tanioka, Y., & Satake, K. (1996). Tsunami generation by horizontal displacement of ocean bottom. *Geophysical Research Letters*, 23(8), 861–864. <https://doi.org/10.1029/96gl00736>
- Tanioka, Y., & Seno, T. (2001). Sediment effect on tsunami generation of the 1896 Sanriku tsunami earthquake. *Geophysical Research Letters*, 28(17), 3389–3392. <https://doi.org/10.1029/2001gl013149>
- Tappin, D. R., Grilli, S. T., Harris, J. C., Geller, R. J., Masterlark, T., Kirby, J. T., et al. (2014). Did a submarine landslide contribute to the 2011 Tohoku tsunami? *Marine Geology*, 357, 344–361. <https://doi.org/10.1016/j.margeo.2014.09.043>
- Tsuru, T., Park, J., Miura, S., Kodaira, S., Kido, Y., & Hayashi, T. (2002). Along-arc structural variation of the plate boundary at the Japan Trench Margin: Implication of interplate coupling. *Journal of Geophysical Research*, 107(B12), 2357. <https://doi.org/10.1029/2001jb001664>
- Wang, X., & Power, W. (2011). COMCOT: A tsunami generation propagation and run-up model. GNS Science Report, New Zealand.
- Wilson, A., & Ma, S. (2021). Wedge plasticity and fully coupled simulations of dynamic rupture and tsunami in the Cascadia subduction zone. *Journal of Geophysical Research: Solid Earth*, 126. <https://doi.org/10.1029/2020JB021627>
- Yamanaka, Y., & Nakamura, M. (2020). Frequency-dependent amplification of the Sanriku tsunamis in Ryori bay. *Earth, Planets and Space*, 72(1). <https://doi.org/10.1186/s40623-019-1128-1>
- Yamazaki, Y., Cheung, K. F., & Lay, T. (2018). A self-consistent fault slip model for the 2011 Tohoku earthquake and tsunami. *Journal of Geophysical Research: Solid Earth*, 123(2), 1435–1458. <https://doi.org/10.1002/2017jb014749>
- Young, D. M. (1971). *Iterative solution of large linear systems*. Academic Press.